Nonlinear optical response of relativistic energy bands

Application to phosphorene

Pedersen, Thomas Garm

Published in:
Physical Review B

DOI (link to publication from Publisher):
10.1103/PhysRevB.95.235419

Publication date:
2017

Document Version
Publisher's PDF, also known as Version of record

Nonlinear optical response of relativistic energy bands: Application to phosphorene

Thomas Garm Pedersen*
Department of Physics and Nanotechnology, Aalborg University, DK-9220 Aalborg Øst, Denmark
and Center for Nanostructured Graphene (CNG), DK-9220 Aalborg Øst, Denmark
(Received 5 April 2017; revised manuscript received 17 May 2017; published 12 June 2017)

The energy dispersion relation of massive relativistic particles is characterized by a gradual transition from parabolic to linear momentum dependence. A similar pseudorelativistic behavior is found in the energy bands of certain two-dimensional semiconductors. Focusing on phosphorene, we investigate the response of pseudorelativistic electrons to electromagnetic fields. It is demonstrated that a near-analytical expression for the induced current containing the field to all orders can be obtained. We analyze the harmonic content of the current and study the field-, frequency-, and band-gap dependence of the nonlinear response. A detailed analysis of third-harmonic generation and saturable absorption is made.

DOI: 10.1103/PhysRevB.95.235419

I. INTRODUCTION

The intense research in two-dimensional materials has uncovered several cases of pseudorelativistic band structures. By far the most prominent example is graphene, in which carriers behave as massless Dirac fermions [1]. This picture emerges from the band structure, which resembles a perfect cone near the so-called "Dirac point" so that the energy depends linearly on momentum. Several instances of isotropic massive Dirac fermions have been discovered including graphene/boron-nitride heterostructures [2] and nanostructured graphene [3–6]. A newcomer to this family is phosphorene, in which carriers to a good approximation behave as anisotropic massive Dirac fermions. Hence, along the armchair direction (x in Fig. 1) the band structure is that of a massive (but light) Dirac fermion, whereas the effective mass of carriers in the zigzag direction (y in Fig. 1) is quite large [7–10]. This difference in carrier character manifests itself in the form of highly anisotropic optical and electronic properties [11–15]. The linear optical response of phosphorene has been studied both experimentally [12,13] and theoretically [14,15], revealing pronounced absorption near the band gap for the armchair direction, in contrast to a near transparency for the zigzag direction.

Recently, the nonlinear optical response of phosphorene has been measured [16–18]. Hence, strong third-order nonlinearities have been found in saturable absorption [16] and third-harmonic generation [17,18]. These results call for a theoretical interpretation of the nonlinear response and, in particular, the role of the unusual band structure. A full theoretical investigation of phosphorene nonlinearities would involve both inter- and intraband contributions [19,20]. In the present work, we focus on the intraband part that is expected to dominate the low-frequency response of doped material. If only a single band is involved, the nonlinear response at arbitrary order can be obtained almost analytically. In fact, in the relaxation-time approximation, the quantum density matrix and the semiclassical Boltzmann formalisms lead to identical results. Thus, we utilize the recent semiclassical analytical formulation by Peres *et al.* [21] and Mikhailov [22] in the present work. As shown by Mikhailov, the optical response of a parabolic band is strictly linear independently of the field strength [22]. A pseudorelativistic energy band, in contrast, leads to nonlinearities of all orders. We verify that, in phosphorene, all odd orders are present while even orders vanish as expected for a centrosymmetric material. Moreover, we investigate the relative intensities of harmonics in high-harmonic generation as a function of field frequency and intensity. We provide a numerical estimate for the magnitude of the intraband third-harmonic generation response and compare to the purely interband contribution.

II. THEORETICAL FRAMEWORK

We start by briefly recapitulating the essential properties of the phosphorene band structure. We will focus on the monolayer case but the important conclusions hold for few-layer and bulk structures as well. In Fig. 1, the phosphorene band structure in the π- electron approximation is displayed. It has been computed using density-functional-based tight binding [23] in a p_z- orbital basis [24,25], but qualitatively similar results are found in density-functional theory [26]. We have used bulk parameters [27] for the monolayer geometry and taken the covalent radius needed in the tight-binding parametrization to be 2.08 Å. In the present context, the crucial feature is the pseudorelativistic energy bands, in particular, along the $\Gamma \rightarrow X$ direction. Thus, both valence and conduction bands are initially (near Γ) parabolic, but quickly become nearly linear, the hallmark of Dirac fermions. The effective electron and hole masses for the $\Gamma \rightarrow X$ direction are found to be 0.176 and 0.182, respectively, in units of the free-electron mass. The corresponding values for the $\Gamma \rightarrow$ Y direction are much greater, i.e., 1.27 and 1.30, respectively.

The dispersion of the lowest conduction and highest valence bands versus momentum $\vec{p}$ is readily rationalized using a two-band pseudorelativistic Hamiltonian. In terms of the Pauli matrices σ_i, a two-dimensional material with anisotropic

*tgp@nano.aau.dk

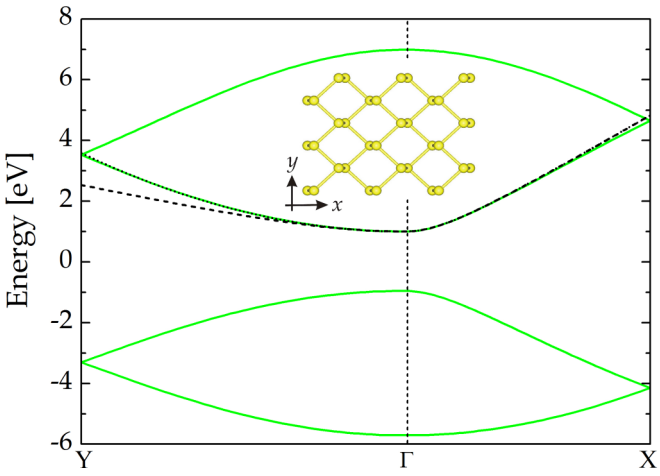

FIG. 1. Tight-binding band structure of monolayer phosphorene (solid lines). The dotted and dashed lines are fits to relativistic energy bands. The atomic structure is shown in the inset.

band velocities and a momentum-dependent mass term is characterized by the Hamiltonian

$$H = v_x p_x \sigma_x + v_y p_y \sigma_y + \Delta(\vec{p})\sigma_z = \begin{pmatrix} \Delta(\vec{p}) & v_x p_x - i v_y p_y \\ v_x p_x + i v_y p_y & -\Delta(\vec{p}) \end{pmatrix}, \quad (1)$$

with eigenvalues $E = \pm\sqrt{\Delta^2(\vec{p}) + v_x^2 p_x^2 + v_y^2 p_y^2}$. An extremely accurate fit to the tight-binding conduction band can be found by taking $\Delta(\vec{p}) = \Delta + w_y^2 p_y^2$ and is shown by the dotted line in Fig. 1. Unfortunately, the quartic term appearing in the energy dispersion renders an analytical approach to the nonlinear response impossible. However, we focus in the present work exclusively on dilutely doped samples, for which the Fermi level is close to the band edge. Thus, we may approximate by taking $\Delta(\vec{p}) = \Delta$ a constant independent of momentum. The fit shown by the dashed line in Fig. 1 yields $\Delta = 1.0$ eV, $v_x \approx 1.0\times10^6$ m/s, and $v_y \approx 0.37\times10^6$ m/s. Below, we show that for x-polarized light the parameter v_y enters into the results only via the doping density n. As the current is simply proportional to n, the value of v_y is unimportant for the relative intensity of harmonic orders. We will ignore excitonic effects in the present work assuming that free carriers introduced through doping will effectively screen the Coulomb effects.

We proceed by discussing the connection between the semiclassical Boltzmann approach and the full quantum-mechanical one. Generally, both intraband and interband transitions contribute to the optical response. A convenient tool to describe these contributions as well as their mixing is provided by the density-matrix ρ formalism [19,20]. For a two-band system consisting of a valence (v) and conduction (c) band, the entries in this matrix are the diagonal band populations $f_v = \rho_{vv}$ and $f_c = \rho_{cc}$ as well as the coherence $\rho_{cv} = \rho_{vc}^*$. Their time evolution is governed by the Liouville equation describing the coupling to the optical field $\vec{F}(t)$, which we take to be polarized along the x direction, i.e., $\vec{F} = F\hat{x}$. Decoherence can be added to the dynamics in various ways. In the relaxation time approximation, it is assumed that the density-matrix elements relax toward their thermal equilibrium values with a characteristic decay rate. As such, the coherence vanishes in thermal equilibrium whereas the populations are given by the Fermi-Dirac distribution $f_0(\vec{p})$ that depends on momentum via the energy $E_{v,c}(\vec{p})$. In the absence of Coulomb effects, the Liouville equations for coherence and conduction band population read as [19,20,28]

$$\frac{\partial \rho_{cv}}{\partial t} + i\omega_{cv}\rho_{cv} = \frac{ieF(t)}{\hbar} x_{cv}(f_c - f_v) + eF(t) \times \left\{ \frac{i}{\hbar}(\Omega_{cc} - \Omega_{vv})\rho_{cv} + \frac{\partial \rho_{cv}}{\partial p_x} \right\} - \tilde{\gamma}\rho_{cv}, \quad (2)$$

and

$$\frac{\partial f_c}{\partial t} = \frac{ieF(t)}{\hbar}(x_{vc}\rho_{cv} - x_{cv}\rho_{vc}) + eF(t)\frac{\partial f_c}{\partial p_x} - \gamma(f_c - f_0). \quad (3)$$

Here, $\hbar\omega_{cv} = E_c - E_v$ is the band-to-band transition energy and x_{cv} is the interband dipole matrix element. Also, Ω_{ii} is the Berry connection and, finally, γ and $\tilde{\gamma}$ are phenomenological relaxation rates for the conduction band population and the coherence, respectively. An equation analogous to Eq. (3) can be written for the valence band population.

We now make the crucial assumption that intraband contributions dominate. This scenario is expected to be realistic provided (i) the material is doped such that the Fermi level lies within a band or close to the band edge, (ii) the optical photon energy $\hbar\omega$ is much smaller than the band gap (1.95 eV in the present model; see Fig. 1). We assume n doping in accordance with recent experimental work [29] so that the relevant band is the conduction band. Hence, ignoring completely all effects of the valence band leads to

$$\frac{\partial f_c}{\partial t} = eF(t)\frac{\partial f_c}{\partial p_x} - \gamma(f_c - f_0). \quad (4)$$

This equation is identical to the semiclassical one studied by Peres *et al.* [21] and Mikhailov [22] and we will adopt the explicit solution given in Refs. [21,22] here. Briefly, Eq. (4) is Fourier transformed in momentum, which leads to a first-order differential equation in time. This equation is solved using standard techniques and the solution is then transformed back to momentum space. This in turn leads to the current

$$j_x(t) = -\frac{e\gamma g}{4\pi^2\hbar^2}\int \frac{\partial E}{\partial p_x}\int_{-\infty}^{t} f_0(\vec{p} + e\vec{\mathcal{A}}(t,t')) \times e^{-\gamma(t-t')}dt'd^2p. \quad (5)$$

Here, $g = 2$ is the spin degeneracy and, assuming a monochromatic field $F(t) = -\mathcal{E}_0 \sin\omega t$, we have the vector potential $\vec{\mathcal{A}}(t,t') = -\int_{t'}^{t}\vec{F}(t'')dt'' = -\hat{x}(\mathcal{E}_0/\omega)(\cos\omega t - \cos\omega t')$. In the case of a pseudorelativistic energy band following Eq. (1), the current becomes

$$j_x(t) = -\frac{e\gamma g v_x^2}{4\pi^2\hbar^2}\int \frac{p_x}{\sqrt{\Delta^2 + v_x^2 p_x^2 + v_y^2 p_y^2}} \times \int_{-\infty}^{t} f_0(\vec{p} + e\vec{\mathcal{A}}(t,t'))e^{-\gamma(t-t')}dt'd^2p. \quad (6)$$

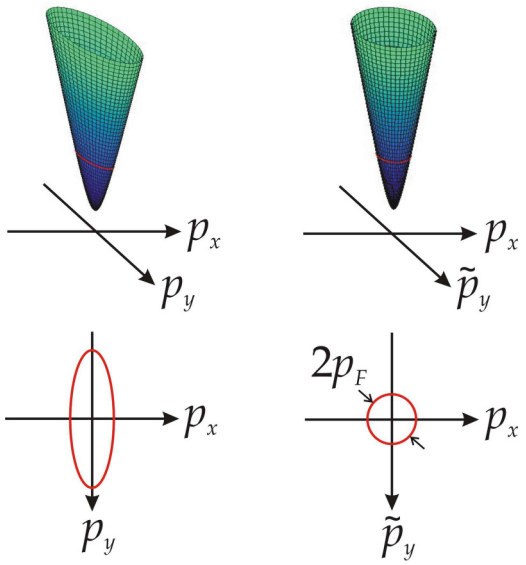

FIG. 2. Transformation of the anisotropic Dirac cone into an isotropic one by scaling of the y momentum.

In order to evaluate this integral, it is convenient to introduce a scaled p_y coordinate given by $\tilde{p}_y = (v_y/v_x)p_y$. As illustrated in Fig. 2, this transforms the anisotropic Dirac cone into an isotropic one. Moreover, the Fermi level now produces a circle rather than an ellipse in momentum space. The radius of this circle is the Fermi momentum p_F as shown in Fig. 2.

In addition, we write $\tilde{p}_x = p_x + e\mathcal{A}(t,t')$ so that

$$j_x(t) = -\frac{e\gamma g v_x^3}{4\pi^2\hbar^2 v_y}\int_{-\infty}^{t}\int \frac{\tilde{p}_x - e\mathcal{A}}{\sqrt{\Delta^2 + v_x^2(\tilde{p}_x - e\mathcal{A})^2 + v_x^2\tilde{p}_y^2}} \times f_0(\tilde{p}_x,\tilde{p}_y)d^2\tilde{p}e^{-\gamma(t-t')}dt'. \quad (7)$$

This form clearly demonstrates the importance of the relativistic energy dispersion for the harmonic content of the current. Thus, for a Schrödinger fermion with parabolic dispersion, the square root in the denominator above is replaced by the constant Δ. Considering then the factor $\tilde{p}_x - e\mathcal{A}$ in the numerator, only the last (field-dependent) term contributes to the current because $f_0(\tilde{p}_x,\tilde{p}_y)$ is an even function of $\tilde{p}_x$. In turn, this demonstrates that the full current becomes proportional to $\mathcal{E}_0$ and hence the response is strictly linear in the field.

Next, we turn to the evaluation of Eq. (7) and the detailed role of the relativistic energy dispersion. In the low-temperature limit, the Fermi-Dirac distribution is a step function $f_0(\tilde{p}_x,\tilde{p}_y) = \Theta(p_F^2 - \tilde{p}^2)$ with $v_x p_F = (E_F^2 - \Delta^2)^{1/2}$. We normalize by the Fermi momentum and write $x = \tilde{p}_x/p_F$, $y = \tilde{p}_y/p_F$, $\Pi = -e\mathcal{A}/p_F$, and $\delta = \Delta/v_x p_F$ so that

$$j_x(t) = -\frac{e\gamma g v_x^2 p_F^2}{4\pi^2\hbar^2 v_y}\int_{-\infty}^{t}\int \frac{x+\Pi}{\sqrt{\delta^2 + (x+\Pi)^2 + y^2}} \times \Theta(1-x^2-y^2)dxdye^{-\gamma(t-t')}dt'. \quad (8)$$

This expression is mathematically identical to the ones derived in Refs. [21,22] except for the δ term in the square root. The prefactor can be related to the electron density given by

$$n = \frac{g}{4\pi^2\hbar^2}\int f_0(\vec{p})d^2p = \frac{g v_x}{4\pi\hbar^2 v_y}p_F^2. \quad (9)$$

Hence,

$$j_x(t) = -\frac{en\gamma v_x}{\pi}\int_{-\infty}^{t}\int \frac{x+\Pi}{\sqrt{\delta^2 + (x+\Pi)^2 + y^2}} \times \Theta(1-x^2-y^2)dxdye^{-\gamma(t-t')}dt'. \quad (10)$$

We introduce $s = \gamma(t-t')$ and write $\mathcal{A}(t,t') = (2\mathcal{E}_0/\omega)\sin(\omega s/2\gamma)\sin[\omega t - (\omega s/2\gamma)]$. Hence, $\Pi = -a\sin z$, where $a = (2\gamma\mathcal{F}/\omega)\sin(\omega s/2\gamma)$ with $\mathcal{F} = e\mathcal{E}_0/(\gamma p_F)$ and $z = [\omega t - (\omega s/2\gamma)]$. In this manner, doing the momentum integral as in Ref. [22] leads to

$$j_x(t) = env_x\int_0^{\infty}\frac{a\sin z}{\sqrt{1+\delta^2+a^2\sin^2 z}} \times {}_2F_1\left[\frac{1}{4},\frac{3}{4},2;\left(\frac{2a\sin z}{1+\delta^2+a^2\sin^2 z}\right)^2\right]e^{-s}ds. \quad (11)$$

This result provides a near-analytical expression for the current including contributions from all orders in the field. From the dependence on the field via a it is apparent that only odd orders appear. To extract particular Fourier components, we follow Mikhailov [22] and introduce generalized conductivities σ_{2m+1} with m a non-negative integer. Hence, the amplitude of the current component oscillating at a frequency $\omega_{2m+1} = (2m+1)\omega$ is written as $j_{2m+1} = \sigma_{2m+1}\mathcal{E}_0$ with

$$\begin{aligned}\sigma_{2m+1} &= \frac{env_x}{\mathcal{E}_0}\int_0^{\infty} aB_{2m+1}(a)\exp\left(i\frac{\omega_{2m+1}s}{2\gamma}\right)e^{-s}ds \\ &= \sigma_0\frac{2\gamma}{\omega}\int_0^{\infty}B_{2m+1}\left[\frac{2\gamma\mathcal{F}}{\omega}\sin\left(\frac{\omega s}{2\gamma}\right)\right]\sin\left(\frac{\omega s}{2\gamma}\right) \\ &\quad\times\exp\left(i\frac{\omega_{2m+1}s}{2\gamma}\right)e^{-s}ds. \quad (12)\end{aligned}$$

Here, $\sigma_0 = e^2 n v_x/(\gamma p_F)$ and

$$B_{2m+1}(a) = \frac{4}{\pi}\int_0^{\pi/2}\frac{\sin z\sin[(2m+1)z]}{\sqrt{1+\delta^2+a^2\sin^2 z}} \times {}_2F_1\left[\frac{1}{4},\frac{3}{4},2;\left(\frac{2a\sin z}{1+\delta^2+a^2\sin^2 z}\right)^2\right]dz. \quad (13)$$

Note that these conductivities are functions of the field strength as well as frequency. To extract low-field perturbative approximations, we utilize the Taylor expansion

$${}_2F_1\left[\frac{1}{4},\frac{3}{4},2;x\right] = 1 + \frac{3}{32}x + \frac{35}{1024}x^2 + O(x^3). \quad (14)$$

Thus, the first three conductivities in the low-field limit $\mathcal{F} \ll 1$ are

$$\sigma_1 = \sigma_0 \frac{\gamma}{(1+\delta^2)^{1/2}(\gamma - i\omega)}, \quad \sigma_3 = \sigma_0 \frac{3\mathcal{F}^2\gamma^3(1+4\delta^2)}{16(1+\delta^2)^{5/2}(\gamma - i\omega)(\gamma - 2i\omega)(\gamma - 3i\omega)},$$
$$\sigma_5 = \sigma_0 \frac{15\mathcal{F}^4\gamma^5(-1-12\delta^2+24\delta^4)}{128(1+\delta^2)^{9/2}(\gamma - i\omega)(\gamma - 2i\omega)(\gamma - 3i\omega)(\gamma - 4i\omega)(\gamma - 5i\omega)}. \tag{15}$$

Near the band edge, i.e., at $E_F = \Delta$, phosphorene is characterized by a nearly parabolic energy dispersion. Hence, the relativistic energy band resembles that of a nonrelativistic Schrödinger fermion. As discussed above, we then expect the nonlinear response to be greatly reduced. The parabolic limit can be reached by increasing the mass term Δ so that $\delta \to \infty$. In this limit, the perturbative expressions in Eq. (15) above show that $\sigma_{2m+1} \propto \delta^{-(2m+1)}$. Hence, the higher harmonics are severely suppressed in this limit, as expected.

In the extreme high-field limit $\mathcal{F} \gg 1$, the δ factor becomes irrelevant and the response approaches that of massless graphene. Hence, the conductivities are approximated by

$$\sigma_{2m+1} \approx \sigma_0 \frac{4}{\pi(2m+1)\mathcal{F}} \int_0^\infty \mathrm{sgn}\left[\sin\left(\frac{\omega s}{2\gamma}\right)\right] \times \exp\left(i\frac{\omega_{2m+1}s}{2\gamma}\right)e^{-s}ds$$
$$= \sigma_0 \frac{4}{\pi(2m+1)\left(1 - i\frac{\omega_{2m+1}}{2\gamma}\right)\tanh\left(\frac{\pi\gamma}{\omega}\right)\mathcal{F}}. \tag{16}$$

Hence, all orders display the same $\mathcal{F}^{-1}$ field dependence in this limit. The sgn[sin(...)] factor is a hallmark of the linear graphene dispersion [30].

It is clear, however, that neglecting interband transitions is no longer valid in the extreme high-field limit. A strong field will induce tunneling across the band gap whenever the field energy is large enough. The intraband regime is restricted by the Keldysh parameter γ_K that is determined by the ratio between energy gap and period-averaged field energy [31]. In the relativistic case [32] adapted to phosphorene,

$$\gamma_K = \frac{m_e v_x \omega}{e\mathcal{E}_0}. \tag{17}$$

Here, $m_e = \Delta/v_x^2$ is the effective band mass. The intraband regime is restricted to $\gamma_K > 1$. In terms of the normalized field, this means $\mathcal{F} < \delta\omega/\gamma \equiv \mathcal{F}_K$. For fields above this limit, the intraband response must be supplemented by interband effects.

To compare the intra- and interband responses, we consider the third-harmonic generation (THG) process. The *purely* interband contribution to THG in an intrinsic two-band semiconductor is given in Ref. [33]. We will take both the incident field and the induced response to be polarized along the armchair direction. Converting dipole to momentum matrix elements, one finds for a two-dimensional system

$$\chi^{(3)}_{\mathrm{inter}} = \frac{ge^4\hbar^2}{\pi^2\varepsilon_0 m^4 d}\int \frac{|p_{vc}|^4}{E_{cv}^3\left(E_{cv}^2 - 9\hbar^2\omega^2\right)\left(E_{cv}^2 - \hbar^2\omega^2\right)}d^2p, \tag{18}$$

with ε_0 the vacuum permittivity and $d = 5.239$ Å the interlayer distance [27]. An analytical estimate can be found if we approximate (i) the interband momentum matrix element p_{vc} by the value at the Γ point p_Γ and (ii) band-to-band transition energy by $E_{cv} \approx 2\sqrt{\Delta^2 + v_x^2p_x^2 + v_y^2p_y^2}$ using the Dirac model. We then find

$$\chi^{(3)}_{\mathrm{inter}} = \frac{ge^4\hbar^2|p_\Gamma|^4}{64\pi\varepsilon_0 m^4 v_x v_y \Delta^5 d} F\left(\frac{\hbar\omega}{2\Delta}\right), \tag{19}$$

where

$$F(z) \equiv \int_0^\infty \frac{x}{(1+x^2)^{3/2}(1+x^2-9z^2)(1+x^2-z^2)}dx$$
$$= \frac{1}{216z^5}\{24z - 27\tanh^{-1}z + \tanh^{-1}3z\}. \tag{20}$$

In the low-frequency limit, $F(z) = \frac{1}{5} + \frac{10}{7}z^2 + O(z^4)$. Using a commutator relation, the momentum matrix element can be written $p_\Gamma = imE_g x_\Gamma/\hbar$, where $E_g \approx 2\Delta$ is the band gap and x_Γ is the transition-dipole moment. From a numerical evaluation using the tight-binding approach, one finds $|x_\Gamma| \approx 4.1$Å close to the armchair lattice constant 4.376 Å [27]. We will apply this approach to evaluate the interband susceptibility below.

III. RESULTS

We aim to apply the theory to phosphorene as a prototypical pseudorelativistic material. In fact, much of the developed theory is rather generic in that the normalized conductivity σ_{2m+1}/σ_0 depends on a very limited number of dimensionless parameters: ω/γ, δ, and $\mathcal{F}$. It is important to bear in mind, though, that the theory is valid only at low photon energies. Hence, assuming a damping rate of $\hbar\gamma = 0.05$ eV the ratio ω/γ should not exceed 20 to keep the photon energy below half the band gap. A damping rate of this magnitude will be assumed in all plots below. Also, a relatively high doping level is required to ensure a dominating intraband response and throughout we will assume that E_F lies 0.1 eV above the conduction band edge Δ. We start by investigating the field dependence of the current harmonics for a fixed frequency. This scenario corresponds to a typical high-harmonic generation experiment, in which a fixed laser frequency is applied. We have considered two cases in Fig. 3: $\hbar\omega = 0.2$ eV (upper panel) and $\hbar\omega = 1.0$ eV (lower panel). At these photon energies, the critical (Keldysh) field strengths are $\mathcal{F}_K \approx 9$ and $\mathcal{F}_K \approx 44$, respectively. At low fields $\mathcal{F} \sim 1$, the conductivities decrease rapidly with order. However, a much more gradual decrease is observed if $\mathcal{F} \sim 50$ or larger. We have included the extreme case $\mathcal{F} = 1000$ in the top panel of Fig. 3 even though this is clearly outside the intraband regime. However, we wish to demonstrate that such an extremely large field is required to approach the asymptotic result [Eq. (16)] shown by stars in Fig. 3. Hence, for realistic field strengths, the response is far from the high-field asymptotic limit. In contrast, for $\mathcal{F} = 1000$

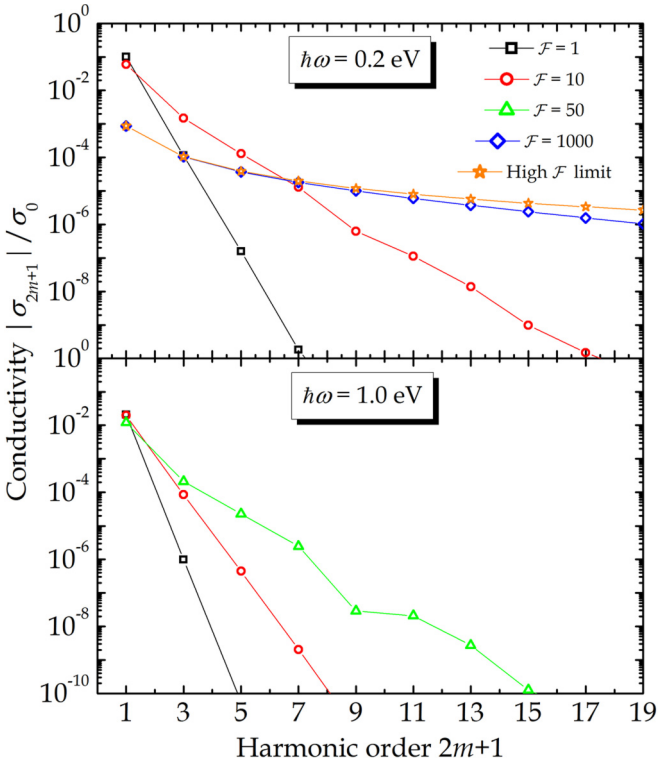

FIG. 3. Generalized conductivities for harmonic order 1 to 19 for a range of field strengths. The photon energy is $\hbar\omega = 0.2$ eV (upper panel) and $\hbar\omega = 1.0$ eV (lower panel).

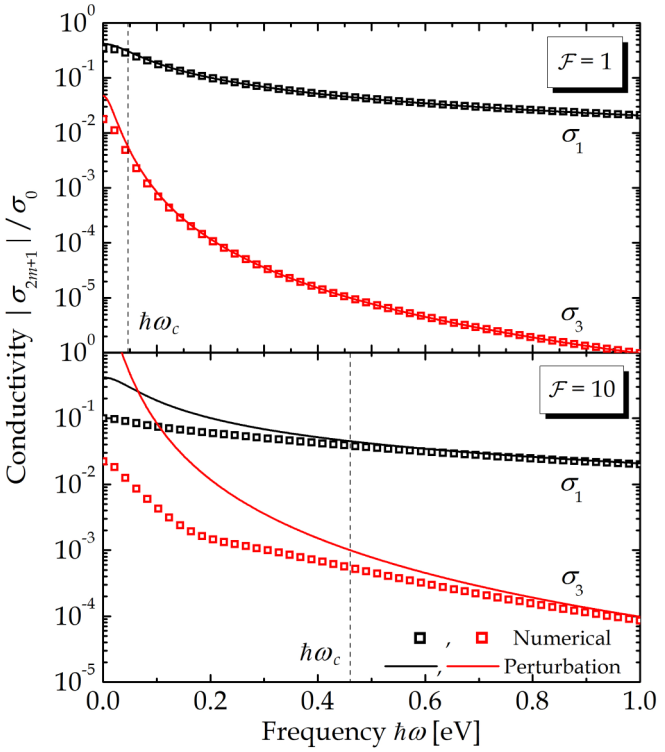

FIG. 4. Frequency dependence of the first and third harmonic response for two different field strengths. Full numerical (symbols) and perturbation results (lines) are compared and the vertical dashed lines indicate the critical frequency.

good agreement between Eq. (16) and the fully numerical results is found, especially for the lower orders. Also, it must be stressed that interband effects are expected to modify the highest harmonics in Fig. 3. Apart from field-induced tunneling across the gap, as discussed above, high photon energies will enable transitions involving remote bands, cf. Fig. 1. Hence, the highest harmonic orders, in particular for $\hbar\omega = 1.0$ eV, are less reliable.

By comparing upper and lower panels in Fig. 3, it is observed that increasing the photon energy leads to a reduced high-harmonic response. The reason for this trend is easily understood from the current expressed in Eq. (6). Hence, the quantity driving the current is the vector potential $\mathcal{A}$ rather than the field. Since $\mathcal{A} \propto \mathcal{E}_0/\omega$ it is, in fact, the ratio of field strength to photon energy that determines the response. Physically, this follows from the rate equation Eq. (4) that relates the time derivative of the electron distribution to the electric field. Thus, upon time integration, the distribution is determined by the integrated field, i.e., the vector potential, rather than the field itself. In Fig. 4, we display the frequency dependence of the first and third harmonic responses for two representative field strengths. In addition to the fully numerical results based on Eq. (12), we include for comparison the perturbative expressions, Eq. (15). In the upper panel, taking $\mathcal{F} = 1$, only extremely low photon energies deviate from the perturbative response. In contrast, taking $\mathcal{F} = 10$ as in the lower panel means that the perturbative regime is only approximately reached for the very highest photon energies considered. The critical frequency $\hbar\omega_c$ defining the perturbative regime (see below) is shown by dashed lines in the plot.

To pinpoint more precisely the field strength required to reach the nonperturbative regime, we plot in Fig. 5 the field dependence of the first and third harmonic for two fixed frequencies. In the perturbative limit, the mth harmonic response varies with field as $\sigma_{2m+1} \propto \mathcal{F}^{2m}$, cf. Eq. (15). Hence, σ_1 and $\sigma_3/\mathcal{F}^2$ are field-independent in this limit. The perturbative predictions are indicated by the solid lines in Fig. 5. Clearly, the full numerics agree with these predictions at low field strength. For a photon energy of $\hbar\omega = 0.2$ eV marked deviations occur at $\mathcal{F} \approx 4$ for both first and third harmonic. In comparison, for the higher frequency of $\hbar\omega = 1.0$ eV the transition is at a much higher field of $\mathcal{F} \approx 20$. Thus, the threshold for nonperturbative behavior is roughly proportional to frequency, in agreement with Fig. 4 and the discussion above. The high-field regime $\mathcal{F} > \mathcal{F}_K$, in which interband dynamics must be included, is shown by the hatched areas in Fig. 5.

The reduction of σ_1 in high fields is a manifestation of saturable absorption similarly to a recent experimental observation [16]. A simple picture of this phenomenon is found by expanding σ_1 from Eq. (12) to second order in $\mathcal{F}$

$$\sigma_1 = \sigma_0 \left\{ \frac{\gamma}{(1+\delta^2)^{1/2}(\gamma - i\omega)} - \frac{9\mathcal{F}^2\gamma^3(1+4\delta^2)}{16(1+\delta^2)^{5/2}(\gamma^2+\omega^2)(\gamma - 2i\omega)} \right\} \approx \frac{i\sigma_0\gamma}{\delta\omega}\left\{1 - \frac{9\mathcal{F}^2\gamma^2}{8\delta^2\omega^2}\right\}. \quad (21)$$

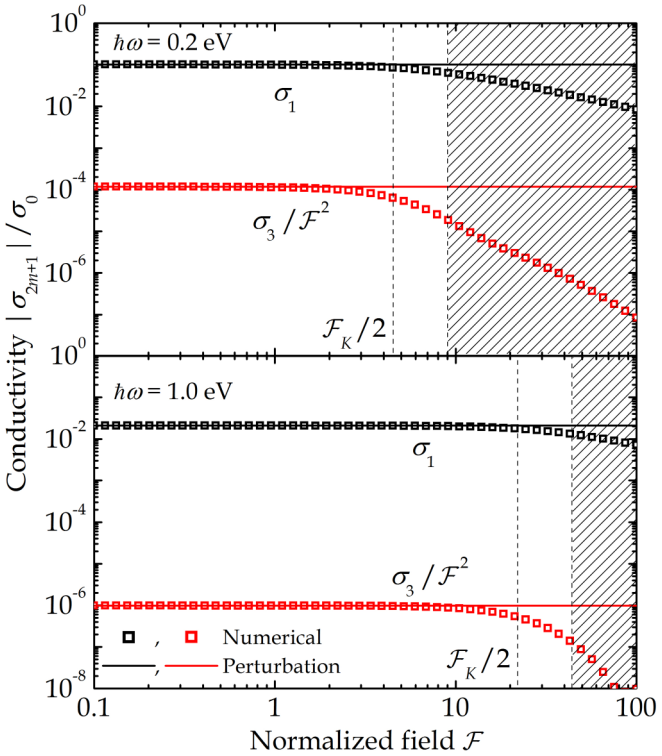

FIG. 5. First and third harmonic response versus normalized field strength for fixed photon energies 0.2 and 1.0 eV. Solid lines and symbols are perturbative and numerical results, respectively. Vertical dashed lines indicate critical fields $\mathcal{F}_K/2$ and hatched areas indicate $\mathcal{F} > \mathcal{F}_K$.

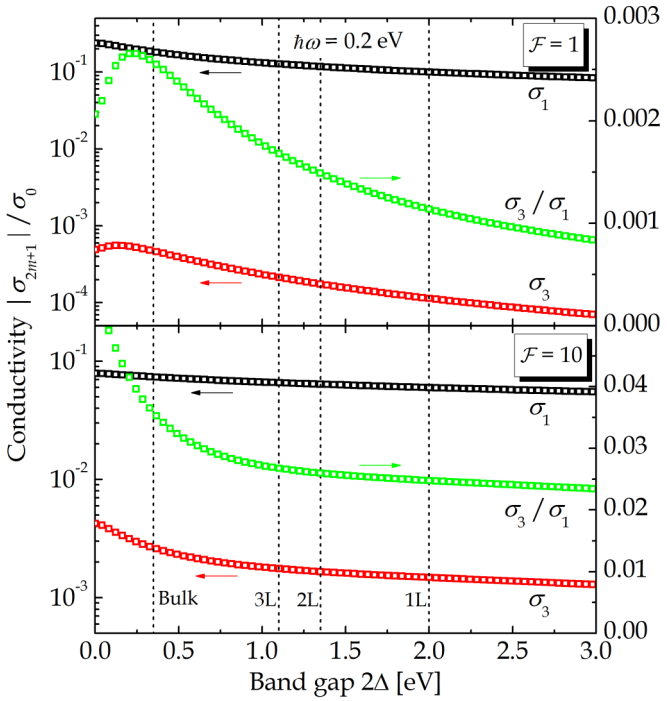

FIG. 6. Response functions versus band gap for low and high fields. The vertical dashed lines indicate quasiparticle gaps of few-layer and bulk phosphorene. The right-hand axes display the ratio σ_3/σ_1.

Here, the first term is identical to Eq. (15), whereas the second is the dominant field-dependent correction at moderate field strengths. The approximate expression in Eq. (17) follows by assuming $\omega \gg \gamma$ and $\delta \gg 1$. The relative minus sign between the two terms is responsible for the reduced response. In terms of the Keldysh critical field, the factor in the braces can be written as $1 - 9\mathcal{F}^2/8\mathcal{F}_K^2$. This factor then readily provides a measure of the critical field strength $\mathcal{F}_c$ required to reach saturable absorption. Hence, if one takes $\mathcal{F}_c \approx \mathcal{F}_K/2$ corresponding to a reduction by a factor $23/32 \approx 0.72$ an excellent agreement with the onsets in Fig. 5 is observed. Note that the same estimate applies to the departure from perturbative behavior in Fig. 4. Thus, by solving the condition $\mathcal{F} = \mathcal{F}_K/2$ for the frequency at a fixed field $\mathcal{F}$, the critical frequency is $\omega_c \approx 2\gamma\mathcal{F}/\delta$ and we find $\hbar\omega_c \approx 0.046$ and $\hbar\omega_c \approx 0.46$ eV for $\mathcal{F} = 1$ and $\mathcal{F} = 10$, respectively, in accordance with Fig. 4.

As discussed above, the harmonic content of the response is highly sensitive to the relativistic nature of the band. A parabolic Schrödinger band leads to a strictly linear response whereas all odd orders are present in the relativistic case. The transition to a nonrelativistic (parabolic) regime can be probed by varying the mass term Δ. Physically, this corresponds to a variation of the band gap $E_g \approx 2\Delta$. The band gap of phosphorene sheets varies strongly with the number of layers. Hence, for mono-, bi-, and trilayers the quasiparticle gaps are approximately 2.0, 1.35, and 1.1 eV, respectively, and in the bulk limit the gap is as small as 0.35 eV [14]. If we ignore the influence of coupling between layers on the optical properties (apart from the influence via the band gap) the response per layer can be calculated using the present framework. In Fig. 6, we have studied the dependence of the optical response on the band gap. This allows us to compare the response of various structures of experimental relevance but, equally important, to probe the transition from the relativistic (linear) to the nonrelativistic (parabolic) regime. We also include the ratio σ_3/σ_1 that is a simple measure of the (high-) harmonic content of the response. As the figure demonstrates, this ratio decreases with band gap apart from a slight exception at very small values of Δ in the low-field case. Also, the decrease is somewhat slower in the high-field case. The reduction of the higher harmonics relative to the first harmonic as exemplified by σ_3/σ_1 is a manifestation of the transition to the nonrelativistic regime as Δ is increased.

We finish with a brief discussion of the absolute magnitude of the nonlinearity. We focus on third-harmonic generation, for which experimental data exist for monolayers [17] and relatively thick multilayer samples [18]. For decoupled layers described by a conductivity σ_3, the associated bulk susceptibility is $\chi^{(3)} = \sigma_3/(3i\omega d\varepsilon_0\mathcal{E}_0^2)$, with ε_0 the vacuum permittivity and $d = 5.239$ Å the interlayer distance [27]. In the perturbative limit and assuming $\omega \gg \gamma$ as well as $\delta \gg 1$, Eq. (15) yields

$$\chi^{(3)}_{\text{intra}} = \frac{e^4 v_x^4 n}{24 d \Delta^3 \omega^4 \varepsilon_0}. \tag{22}$$

To provide an estimate, we take $\Delta = \hbar\omega = 0.35$ eV. Hence, for a doping density $n = 10^{15}$ m^{-2}, we find the

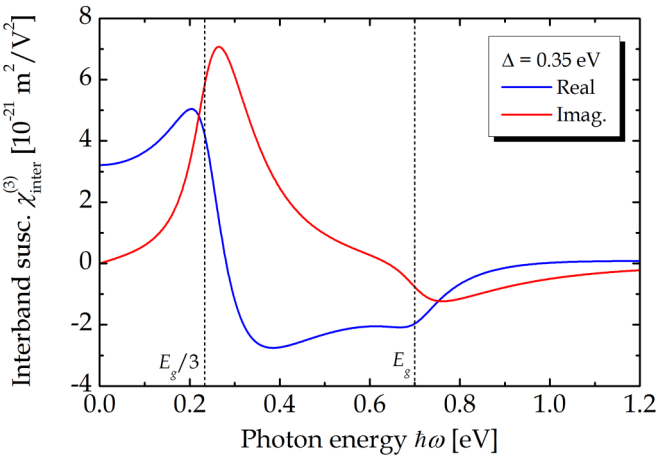

FIG. 7. Purely interband contribution to the third harmonic response assuming $\Delta = 0.35$ eV. The dashed lines indicate ω and 3ω resonances.

estimate $\chi^{(3)}_{\rm intra} = 4.1\times10^{-19}$ m^2/V^2 of similar magnitude as the measured value 1.4×10^{-19} m^2/V^2 in Ref. [18]. Hence, we conclude that provided sufficient doping densities can be reached, the predicted intraband response found in the present work can, indeed, be of a significant magnitude.

Additionally, we may estimate the purely interband contribution to $\chi^{(3)}$ using Eq. (19) and assuming $\Delta = 0.35$ eV similarly to the intraband estimate above. The result is illustrated in Fig. 7, highlighting the ω and 3ω resonances. Even though a significant dispersion is observed, one finds an interband response below $|\chi^{(3)}_{\rm inter}| < 10^{-20}$ m^2/V^2 throughout the spectrum. Thus, the interband contribution is expected to be significant but less than the intraband one. It must be remembered that, in addition to the two contributions investigated here, *mixed* response functions exist [33] and these may possibly exceed the purely intraband contribution.

IV. SUMMARY

In this paper, the nonlinear intraband optical response of electrons in pseudorelativistic energy bands has been computed. A semianalytical calculation including all harmonic orders has been presented and applied to phosphorene. In addition, approximate harmonic response functions for the low- and high-field regimes have been derived. We demonstrate that the relativistic nature of the band structure is crucial for the nonlinear response, which vanishes identically in the strictly nonrelativistic limit of parabolic bands. The frequency and field dependence of the optical response reveals that nonperturbative behavior sets in above a certain threshold field strength. Hence, as applications of the theory, simple expressions for the third-harmonic response as well as the threshold for saturable absorption are derived.

ACKNOWLEDGMENTS

This work is financially supported by the Center for Nanostructured Graphene (CNG) and the QUSCOPE center. CNG is sponsored by the Danish National Research Foundation, Project DNRF103 and QUSCOPE is sponsored by the Villum Foundation.

[1] A. H. Castro Neto, F. Guinea, N. M. R. Peres, K. S. Novoselov, and A. K. Geim, Rev. Mod. Phys. **81**, 109 (2009).
[2] B. Hunt, J. D. Sanchez-Yamagishi, A. F. Young, M. Yankowitz, B. J. LeRoy, K. Watanabe, T. Taniguchi, P. Moon, M. Koshino, P. Jarillo-Herrero, and R. C. Ashoori, Science **340**, 1427 (2013).
[3] J. A. Fürst, J. G. Pedersen, C. Flindt, N. A. Mortensen, M. Brandbyge, T. G. Pedersen, and A.-P. Jauho, New J. Phys. **11**, 095020 (2009).
[4] J. G. Pedersen, T. Gunst, T. Markussen, and T. G. Pedersen, Phys. Rev. B **86**, 245410 (2012).
[5] J. G. Pedersen and T. G. Pedersen, Phys. Rev. B **87**, 235404 (2013).
[6] D. R. Andersen and H. Raza, J. Phys.: Condens. Matter **25**, 045303 (2013).
[7] M. Ezawa, New J. Phys. **16**, 115004 (2014).
[8] V. Tran and L. Yang, Phys. Rev. B **89**, 245407 (2014).
[9] J. Kim, S. S. Baik, S. H. Ryu, Y. Sohn, S. Park, B.-G. Park, J. Denlinger, Y. Yi, H. J. Choi, and K. S. Kim, Science **349**, 723 (2015).
[10] E. T. Sisakht, M. H. Zare, and F. Fazileh, Phys. Rev. B **91**, 085409 (2015).
[11] H. Liu, A. T. Neal, Z. Zhu, Z. Luo, X. Xu, D. Tománek, and P. D. Ye, ACS Nano **8**, 4033 (2014).
[12] G. Zhang, S. Huang, A. Chaves, C. Song, V. O. Özçelik, T. Low, and H. Yan, Nat. Commun. **8**, 14071 (2017).
[13] L. Li, J. Kim, C. Jin, G. J. Ye, D. Y. Qiu, F. H. da Jornada, Z. Shi, L. Chen, Z. Zhang, F. Yang, K. Watanabe, T. Taniguchi, W. Ren, S. G. Louie, X. H. Chen, Y. Zhang, and F. Wang, Nat. Nanotechnol. **12**, 21 (2017).
[14] V. Tran, R. Fei, and L. Yang, 2D Mater. **2**, 044014 (2015).
[15] X. Wang, A. M. Jones, K. L. Seyler, V. Tran, Y. Jia, H. Zhao, H. Wang, L. Yang, X. Xu, and F. Xia, Nat. Nanotechnol. **10**, 517 (2015).
[16] S. B. Lu, L. L. Miao, Z. N. Guo, X. Qi, C. J. Zhao, H. Zhang, S. C. Wen, D. Y. Tang, and D. Y. Fan, Opt. Express **23**, 11183 (2015).
[17] M. J. L. F. Rodrigues, C. J. S. de Matos, Y. W. Ho, H. Peixoto, R. E. P. de Oliveira, H-Y. Wu, A. H. Castro Neto, and J. Viana-Gomes, Adv. Mater. **28**, 10693 (2016).
[18] N. Youngblood, R. Peng, A. Nemilentsau, T. Low, and M. Li, ACS Photon. **4**, 8 (2017).
[19] C. Aversa and J. E. Sipe, Phys. Rev. B **52**, 14636 (1995).
[20] T. G. Pedersen, Phys. Rev. B **92**, 235432 (2015).
[21] N. M. R. Peres, Yu. V. Bludov, J. E. Santos, A-P. Jauho, and M. I. Vasilevskiy, Phys. Rev. B **90**, 125425 (2014).
[22] S. A. Mikhailov, Phys. Rev. B **95**, 085432 (2017).
[23] D. Porezag, Th. Frauenheim, Th. Köhler, G. Seifert, and R. Kaschner, Phys. Rev. B **51**, 12947 (1995).
[24] T. G. Pedersen, Phys. Rev. B **69**, 075207 (2004).

[25] T. G. Pedersen and J. G. Pedersen, Phys. Rev. B **87**, 155433 (2013).
[26] A. S. Rodin, A. Carvalho, and A. H. Castro Neto, Phys. Rev. Lett. **112**, 176801 (2014).
[27] Y. Takao and A. Morita, Physica B+C (Amsterdam) **105**, 93 (1981).
[28] D. Dimitrovski, L. B. Madsen, and T. G. Pedersen, Phys. Rev. B **95**, 035405 (2017).
[29] R. A. Doganov, S. P. Koenig, Y. Yeo, K. Watanabe, T. Taniguchi, and B. Özyilmaz, Appl. Phys. Lett. **106**, 083505 (2015).
[30] S. A. Mikhailov, Europhys. Lett. **79**, 27002 (2007).
[31] V. Keldysh, Sov. Phys. JETP **20**, 1307 (1964).
[32] B. M. Karnov, V. D. Mur, and V. S. Popov, Laser Phys. **15**, 1556 (2005).
[33] C. Aversa, J. E. Sipe, M. Sheik-Bahae, and E. W. Van Stryland, Phys. Rev. B **50**, 18073 (1994).